Estimation of interval velocity and attenuation anisotropy from reflection data at Coronation Field

Jyoti Behura and Ilya Tsvankin, Colorado School of Mines
Edward Jenner and Alex Calvert, ION Geophysical

Attenuation can be extremely valuable in characterizing gas accumulations in shales and sandstones. Laboratory studies clearly indicate that attenuation is closely related to fluid saturation and mobility. Well-log analysis shows that P-wave attenuation is higher in gas-bearing rocks than in those saturated with oil or water. Extremely low P-wave quality factors (Q), ranging between 5 and 10, have been observed in some gas reservoirs. For example, such low Q values in gas sands are reported by Mavko and Dvorkin (2005) in well logs from the Gulf Coast.

Attenuation anisotropy might carry valuable information about aligned fractures. In fact, preferential flow of fluids in rocks and layering is believed to be the primary cause of attenuation anisotropy (e.g., Behura et al., 2009; Mavko and Nur, 1979). Fluid-flow models show that aligned fluid-filled cracks can result in anisotropic attenuation. Poroelastic modeling can explain strong anisotropic attenuation in the seismic bandwidth. Low-frequency laboratory experiments on oil shales show that as the solid kerogen melts, the shale exhibits stronger attenuation anisotropy (Behura et al., 2009). Low Q values in fractured zones of shale-sand sequences have been found from crosswell studies. These studies also report strong attenuation anisotropy with the vertical attenuation coefficient five times larger than the horizontal coefficient. Vertical seismic profiling (VSP) studies also show attenuation anisotropy attributed to fluid-filled fractures.

Behura and Tsvankin (2009a) introduce a layer-stripping technique to extract interval attenuation from reflection data using velocity-independent layer-stripping (Dewangan and Tsvankin, 2006) and a variation of the spectral-ratio method. While no information about velocity and attenuation anywhere in the medium is required, the overburden has to be laterally homogeneous with a horizontal symmetry plane. Using synthetic examples for VTI (transversely isotropic with a vertical symmetry axis) and orthorhombic models, Behura and Tsvankin (2009a) demonstrate that this algorithm can successfully estimate interval anisotropic attenuation in 2D and 3D. Here, we apply this technique to wide-azimuth data acquired at Coronation Field, Alberta, and investigate the spatial distribution of gas accumulation and fracturing using velocity and attenuation attributes.

Geologic setting

The Coronation Field is a gas reservoir located in east central Alberta (Figure 1). The field is part of the Western Canadian Sedimentary Basin with the hydrocarbon production mostly from the Mannville Group. That group is of Cretaceous age and corresponds to a major episode of subsidence and sedimentation following a long period of uplift, exposure, and erosion of older strata. It overlies a Paleozoic unconformity and is unconformably overlaid by the marine shales of Joli Fou Formation (Colorado Group). The Joli Fou shales form the cap rock, while the Lower Cretaceous shales and coals are believed to be the source of the hydrocarbons. The Mannville Group is usually divided into the Upper and Lower Units based on sandstone lithology (Figure 2); the Lower Unit is richer in quartz and chert while the Upper unit has a more feldspathic and volcanic composition. Besides sandstones, the lithology of the Mannville Group is comprised of nonmarine and minor marine shales, and coal seams. Light oil and gas are usually trapped in numerous fluvial and valley-fill reservoir sandstones, while heavy oil is found in more regionally extensive shoreline sand complexes in the northern and central parts of Alberta and Saskatchewan.

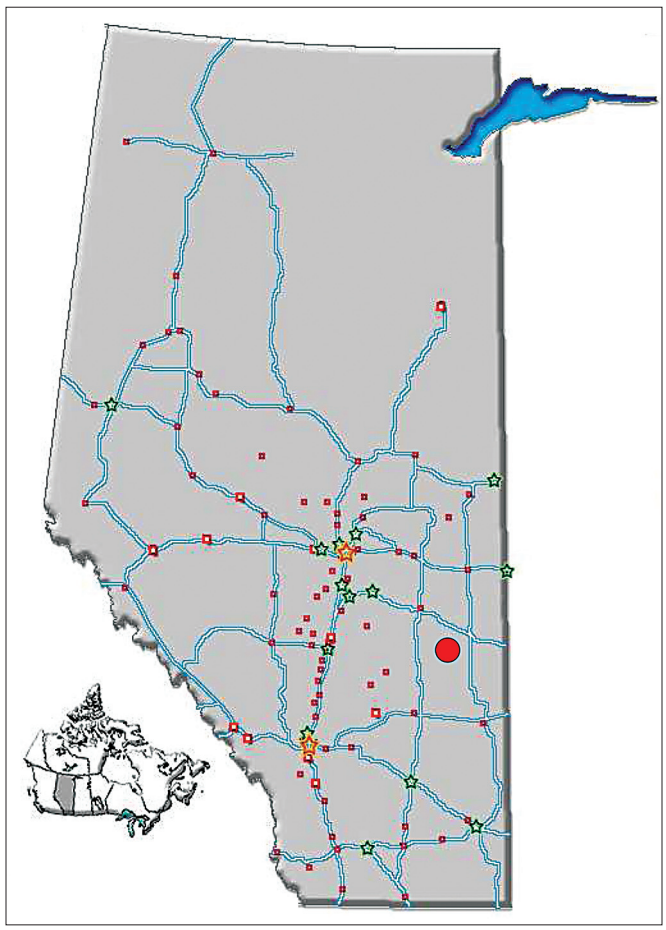

Figure 1. *Location of Coronation Field (red dot) in Alberta, Canada.*

The interval of primary interest at Coronation Field is the Rex member of the Mannville Group (Monk et al., 2006). The sand channels immediately underlie the coals of the Rex member and could vary in thickness from 4 m to 10 m. The width

of these channel systems ranges between 200 m and 300 m. Good producers yield approximately 500 MCF of gas per day with the total production of nearly 0.7 BCF per well. Because of the high cost of developing this field, drilling success is critical.

Velocity-independent layer-stripping algorithm

Dewangan and Tsvankin (2006) show that the interval reflection traveltime for an anisotropic, heterogeneous target layer overlaid by a laterally homogeneous overburden, that has a horizontal symmetry plane, can be reconstructed by a process that involves matching the horizontal slownesses of the target and overburden reflections. Note that the above constraint on the overburden is required to hold only locally (i.e., on the scale of CMP gather) and the algorithm is still valid for long-wavelength lateral heterogeneity in the overburden.

The algorithm aims to identify overburden raypaths *ABD* and *FEG* (Figure 4) that share the downgoing and upgoing legs *AB* and *EG*, respectively, with the target reflection *ABCEG*. The traveltime slope (horizontal slowness) for the target event *ABCEG* at receiver location *G* is first calculated using a shot gather at location *A*. Then we compute the time slope of the overburden reflection for a range of shot points using a receiver gather at location *G*. The shot for which the time slope of the overburden reflection is equal to that of the target event at point *G* yields the sought location *F*. Since the overburden is assumed to be locally laterally homogeneous and the horizontal slownesses at locations *F* and *G* coincide, the raypaths *ABCEG* and *FEG* share the upgoing leg *EG*. Similarly, we identify the overburden raypath *ABD* that shares the downgoing leg *AB* with the target event *ABCEG*.

It follows from the above assumptions about the overburden that the reflection point *B* is the midpoint of locations *A* and *D*, while *E* is the midpoint of *G* and *F* . Then the interval traveltime along the raypath *BCE* can be computed using

$$t_{BCE} = t_{ABCEG} - \frac{t_{ABD} + t_{FEG}}{2}, \qquad (1)$$

where t_{ABCEG}, t_{ABD}, and t_{FEG} are the traveltimes along the raypaths *ABCEG*, *ABD*, and *FEG*, respectively. Further details of the velocity-independent layer stripping method can be found in Dewangan and Tsvankin (2006) and (for 3D wide-azimuth data) Wang and Tsvankin (2009).

Behura and Tsvankin (2009a, b) show that the above algorithm, in combination with the spectral-ratio method, can be adapted to evaluate the offset-dependent interval attenuation in the target layer. The normalized phase attenuation coefficient, $\mathcal{A} = 1/(2Q)$, along the raypath *BCE* can be computed from the following spectral ratio:

$$ln\left(\frac{|U_{ABCEG}(\omega)|^2}{|U_{ABD}(\omega)|\,|U_{FEG}(\omega)|}\right) = lnG - 2\omega\mathcal{A}\,t_{BCE} \qquad (2)$$

where ω is the frequency, $U_{ABCEG}(\omega)$, $U_{ABD}(\omega)$, and $U_{FEG}(\omega)$ are the frequency-domain amplitudes of the corresponding target and overburden reflections, and G includes the source/receiver directivity, scattering coefficients, and geometrical spreading (Behura and Tsvankin, 2009a). Assuming G to be frequency-independent, the attenuation coefficient $\mathcal{A}$ can then be computed from the slope of the spectral ratio ($2\mathcal{A}t_{BCE}$; Equation 2) and the interval traveltime t_{BCE} obtained from the layer-stripping algorithm (Equation 1).

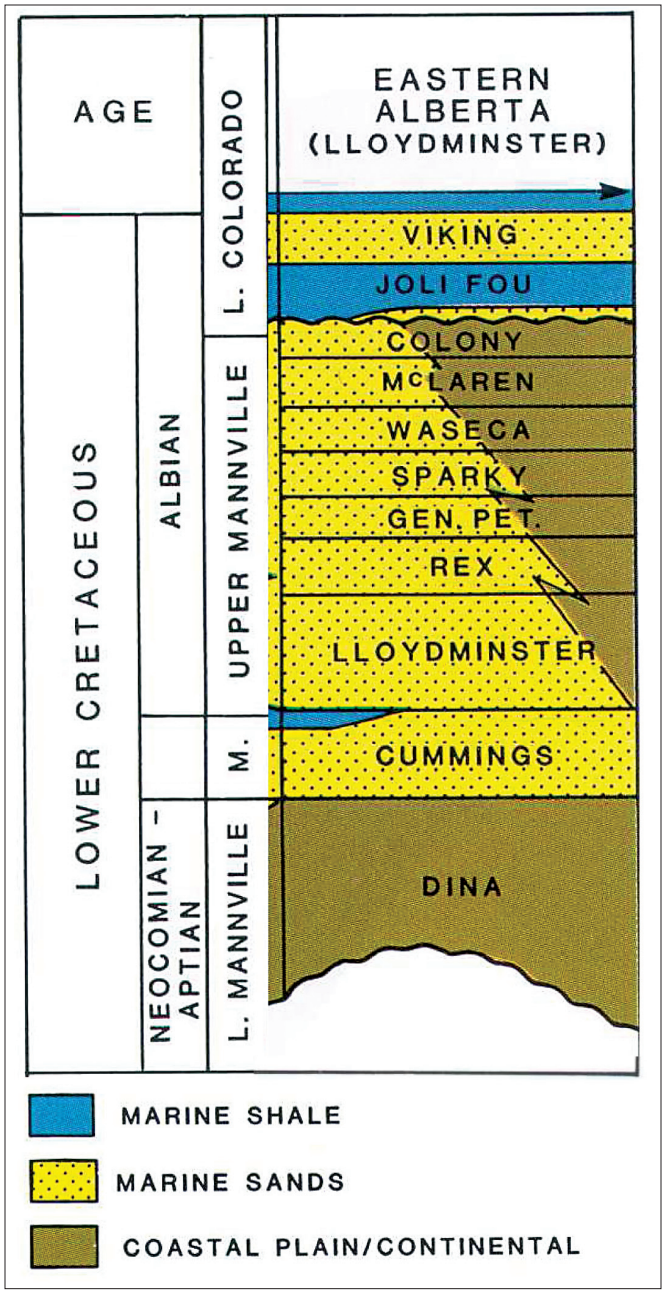

Figure 2. *Stratigraphic column of the regional geology at Coronation Field (Jackson, 1984). The reservoir sandstones of Mannville are bounded by the Joli Fou shales above and the Paleozoic unconformity below.*

Data acquisition and processing

To understand the lithology of the channel sands and help optimize well placement, Apache Corporation acquired a 3D multicomponent seismic survey (the data are currently owned by VGS Seismic Canada). In this study, we use only the verti-

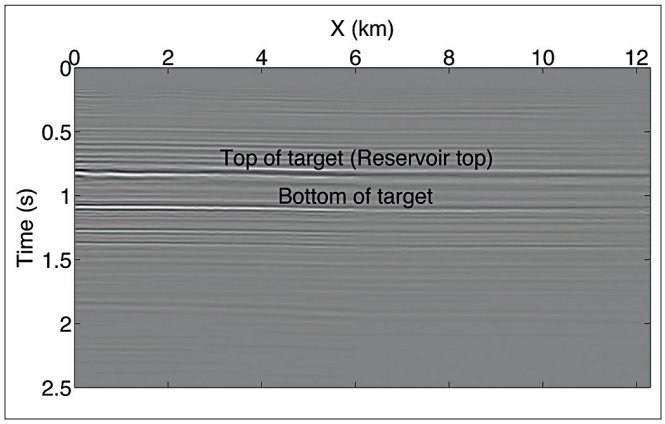

Figure 3. *Seismic section spanning the length of the survey. The marked reflectors bound the interval of interest.*

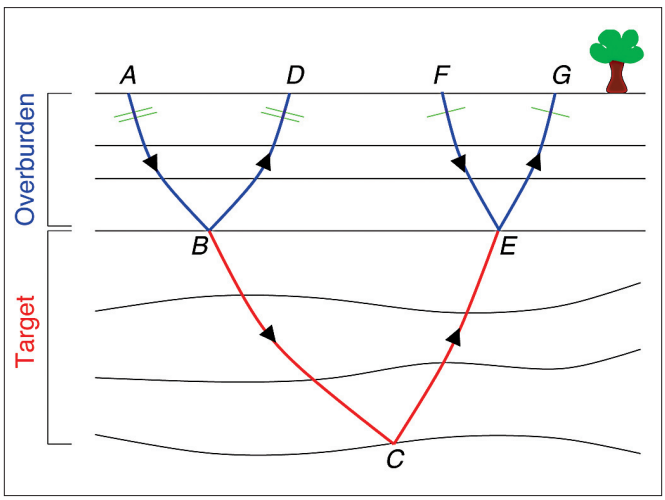

Figure 4. *2D ray diagram of the layer-stripping algorithm. Points B and E are at the bottom of the overburden. The target reflection ABCEG and the reflection ABD from the bottom of the overburden share the downgoing leg AB. The upgoing leg EG of the target event coincides with a leg of another overburden reflection, FEG.*

cal-component data to carry out P-wave velocity and attenuation analysis. The entire survey was shot using single-hole dynamite on a "shoot and roll" template of 12 × 94 receivers (Table 1) with the source at the center of the patch. This shooting template is roughly square, yielding an excellent azimuthal and offset distribution. The shot lines are oblique to the receiver lines, as shown in Figure 5. The subsurface structure is fairly close to layer-cake with almost no structural dip (Figure 3), which facilitates the application of layer-stripping technique described above (Behura and Tsvankin, 2009a).

Prior to attenuation analysis, refraction statics corrections were applied to shift the data to a smooth floating datum. Some traces were subsequently edited to remove spikes and random noise. Denoising was followed by three passes of residual statics corrections. The ground roll was suppressed using *f-k* filtering followed by surface-consistent median gain applied to compensate for the variation in the dynamite source strength.

Interval traveltime. The most critical step in estimating interval parameters is to obtain traveltimes of reflections from the top and bottom of the target layer which can be done using either an autopicker or semblance analysis. Here, we use a 3D nonhyperbolic semblance algorithm for layered orthohombic media based on the generalized Alkhalifah-Tsvankin equation:

Survey type	3C–3D
Shot interval (single-hole dynamite)	42.43 m
Shot line interval	240 m
Receiver interval	30 m
Receiver line interval	210 m
Receiver patch	12 × 94
Total survey shots	11174
Total survey receivers	11255
Nominal fold (30 × 30 m bins)	140
Maximum offset	2060 m

Table 1. *Acquisition parameters of the survey (Monk et al., 2006).*

$$t^2(x,\alpha) = t_0^2 + \frac{x^2}{V_{\mathrm{nmo}}^2(\alpha)} - \frac{2\eta(\alpha)x^4}{V_{\mathrm{nmo}}^2(\alpha)\left[t_0^2\, V_{\mathrm{nmo}}^2(\alpha) + (1+2\eta(\alpha))x^2\right]}, \quad (3)$$

where t is the reflected traveltime, x is the offset, t_0 is the two-way zero-offset traveltime, α is the source-to-receiver azimuth, $V_{\mathrm{nmo}}(\alpha)$ is the azimuthally varying normal-moveout velocity, and $\eta(\alpha)$ is the "anellipticity" coefficient responsible for the deviation from hyperbolic moveout at long offsets. The velocity $V_{\mathrm{nmo}}(\alpha)$ is obtained from the equation of the NMO ellipse:

$$V_{\mathrm{nmo}}^{-2}(\alpha) = \frac{\sin^2(\alpha-\varphi)}{\left[V_{\mathrm{nmo}}^{(1)}\right]^2} + \frac{\cos^2(\alpha-\varphi)}{\left[V_{\mathrm{nmo}}^{(2)}\right]^2}. \quad (4)$$

For a single layer, φ is the azimuth of the $[x_1, x_3]$ symmetry plane, and $V_{\mathrm{nmo}}^{(1)}$ and $V_{\mathrm{nmo}}^{(2)}$ are the NMO velocities in the vertical symmetry planes $[x_2, x_3]$ and $[x_1, x_3]$, respectively. The parameter η depends on the azimuth φ and the anellipticity parameters $\eta^{(1)}$, $\eta^{(2)}$, and $\eta^{(3)}$. The above semblance algorithm is designed to operate on CMP gathers. Implementation of the layer-stripping algorithm described above (Behura and Tsvankin, 2009a), however, requires traveltime surfaces on source and receiver gathers. By assuming not just the overburden, but also the target layer to be locally laterally homogeneous, one can apply semblance analysis based on Equation 3 to source and receiver gathers. Since velocity-independent layer stripping requires the horizontal slowness at both the source and receiver locations, the best-fit effective moveout parameters are computed for the source as well as receiver gathers. The wide-azimuth reflection traveltimes for the top and bottom of the target layer serve as inputs to the layer-stripping method (see above), which produces the interval traveltime, as described by Dewangan and Tsvankin (2006) in 2D and Wang and Tsvankin (2009) for 3D wide-azimuth data.

Assuming the velocity anisotropy to have orthorhombic symmetry, we can use the interval traveltimes obtained by layer stripping to invert for the velocity-anisotropy parameters of the target layer. P-wave reflection traveltimes constrain the moveout parameters $V_{\mathrm{nmo}}^{(1,2)}$, $\eta^{(1,2,3)}$, and φ of the target layer. If the vertical velocity V_{P0} or the thickness of the target layer is known, then the interval anisotropy parameters $\varepsilon^{(1,2)}$ and $\delta^{(1,2,3)}$ (Tsvankin, 1997) can be computed from the moveout parameters using the following expressions:

$$V_{\mathrm{nmo}}^{(1)} = V_{P0}\sqrt{1+2\delta^{(1)}},$$

$$V_{\mathrm{nmo}}^{(2)} = V_{P0}\sqrt{1+2\delta^{(2)}},$$

$$\eta^{(1)} = \frac{\varepsilon^{(1)}-\delta^{(1)}}{1+2\delta^{(1)}},$$

$$\eta^{(2)} = \frac{\varepsilon^{(2)}-\delta^{(2)}}{1+2\delta^{(2)}},$$

$$\eta^{(3)} = \frac{(\varepsilon^{(1)}-\varepsilon^{(2)}-\delta^{(3)})(1+2\varepsilon^{(2)})}{(1+2\varepsilon^{(2)})(1+2\delta^{(3)})}. \quad (5)$$

Interval attenuation. The interval traveltime and windowed events along the moveout surfaces are used to compute the interval attenuation coefficient following the technique of Behura and Tsvankin (2009a). The presence of notches in the source amplitude spectra complicates the Q estimation using the spectral-ratio method. To overcome this problem, we compute the instantaneous Q at every frequency followed by median filtering to eliminate spikes. The resulting average over the Q values is taken as a measure of attenuation along the raypath. The additional advantage of computing the instantaneous Q is that it provides a measure of the variance of the normalized phase attenuation coefficient $\mathcal{A}$.

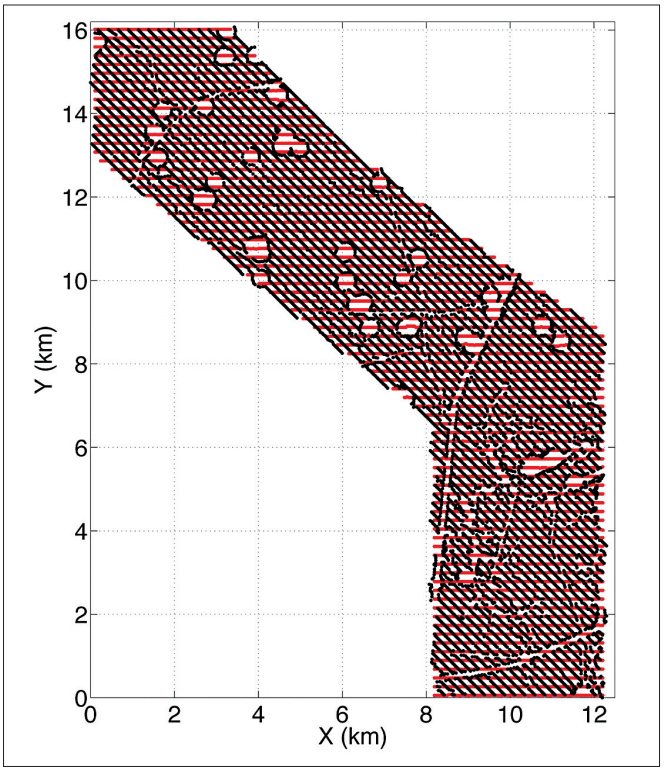

Figure 5. *Seismic acquisition grid for the 3C survey at Coronation Field. The black dots represent the shot locations while the receiver locations are marked with red dots.*

The attenuation-anisotropy parameters are found by fitting the approximate P-wave phase-attenuation function $\mathcal{A}_p$ in orthorhombic media (Zhu and Tsvankin, 2007) to the estimated interval values:

$$\mathcal{A}_P(\theta,\phi) = \mathcal{A}_{P0}\,[1 + \delta_Q(\phi)\sin^2\theta\cos^2\theta + \varepsilon_Q(\phi)\sin^4\theta], \quad (6)$$

where $\mathcal{A}_{P0}$ is the vertical attenuation coefficient, θ and ϕ are the polar and azimuthal phase angles, respectively, and δ_Q and ε_Q are functions of attenuation parameters φ_Q, $\delta_Q^{(1,2,3)}$, and $\varepsilon_Q^{(1,2)}$ (Zhu and Tsvankin, 2007). The angle φ_Q is the azimuth of the $[x_1, x_3]$ symmetry plane (for attenuation) and the parameters $\delta_Q^{(1,2,3)}$ and $\varepsilon_Q^{(1,2)}$ govern the angular variation of the P-wave attenuation coefficient (Zhu and Tsvankin, 2007). We do not assume the same symmetry-plane azimuths for attenuation and velocity anisotropy.

Although Equation 6 describes the angular variation of the phase attenuation coefficient $\mathcal{A}$, it is valid for the group attenuation coefficient $\mathcal{A}_g$ estimated from seismic data (Behura and Tsvankin, 2009b). Inversion for the attenuation-anisotropy parameters requires knowledge of the anisotropic velocity field needed to compute the phase direction from the measured group direction. We use the interval vertical P-wave velocity derived from well logs (V_{P0} = 5000 m/s) to estimate the velocity anisotropy parameters $\delta^{(1,2,3)}$ and $\varepsilon^{(1,2)}$ from the moveout parameters (Equation 5). Using the obtained velocity model, we compute the phase angles from the group angles. Note that it is possible to perform velocity analysis prior to attenuation processing using the interval traveltime because the influence of attenuation on velocity for a fixed frequency typically is of the second order (Behura and Tsvankin, 2009b; Zhu and Tsvankin, 2007).

To compute the variance of the estimated moveout parameters, we assume a 4-ms standard deviation (two times the sampling interval) of the semblance-derived traveltimes. Applying the method of error propagation to Equations 3–5, we calculate the standard deviation of the parameters V_{P0}, $\delta^{(1,2,3)}$, and $\varepsilon^{(1,2)}$.

Since the variance is available for every estimated value of the attenuation coefficient $\mathcal{A}$, we apply the method of weighted least squares to estimate the attenuation-anisotropy parameters and their variances. By using the inverse of the variances as weights, values with a smaller variance are assigned larger weights. The method of error propagation is then employed to calculate the variance-covariance matrix of the attenuation-anisotropy parameters.

Results

Here, we discuss the results of azimuthal velocity and attenuation analysis for an interval starting at about 0.8 s which con-

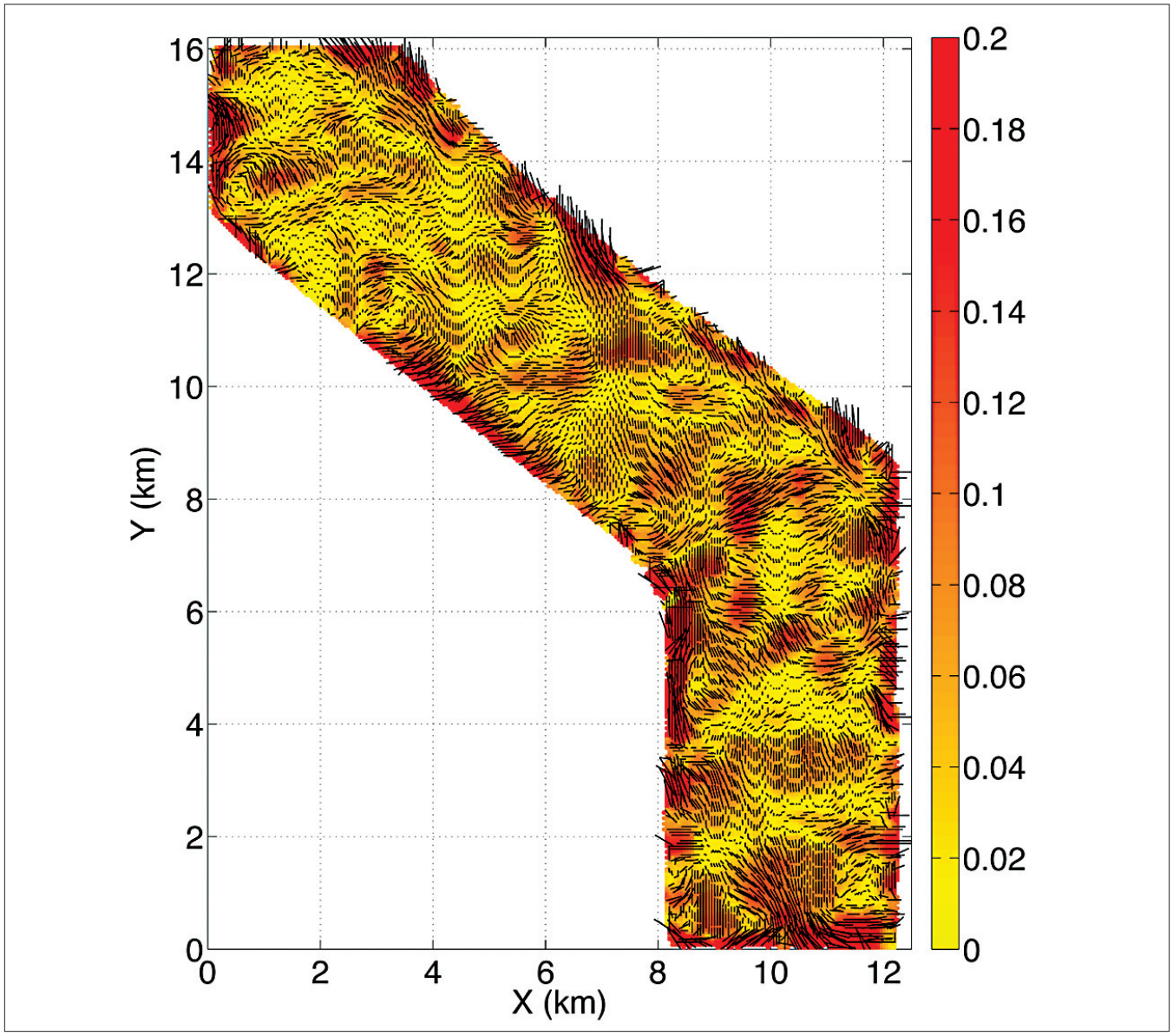

Figure 6. *Eccentricity (tick lengths and color scale) and the azimuth of the major axis (tick directions) of the interval NMO ellipses in the target.*

tains the reservoir (Figure 3). The interval NMO ellipse of the target layer is represented by its eccentricity and the azimuth

of the major axis (Figure 6) for each common midpoint. The NMO eccentricity is defined as $|V_{\mathrm{nmo}}^{(1)} - V_{\mathrm{nmo}}^{(2)}|/V_{\mathrm{nmo}}^{(\mathrm{fast})}$ where $V_{\mathrm{nmo}}^{(\mathrm{fast})} = \max\{V_{\mathrm{nmo}}^{(1)}, V_{\mathrm{nmo}}^{(2)}\}$. Azimuthal velocity anisotropy is substantial (up to 20%) within the target layer and varies smoothly over the field. If the field had only one dominant fracture set, the major axis of the NMO ellipse would be parallel to the fractures and in the areas showing strong azimuthal anisotropy the target layer is more intensely fractured. For increased production from fractured formations, horizontal wells should be drilled orthogonal to the fracture strike. In the presence of more than one fracture set, however, interpretation of NMO ellipses becomes more complicated. Additional data such as well-bore resistivity images could help resolve this ambiguity.

The vertical attenuation coefficient $\mathcal{A}_0$ is displayed in Figure 7. Zones of higher attenuation (hot colors) in the lower half of the survey area show good correlation with locations of existing gas-producing wells (Monk et al., 2006). All the producing wells overlie areas showing high attenuation; on the other hand, two of the dry wells lie on the edge of the high-attenuation zone and one of them is located in an area with extremely low attenuation (Figure 7). Therefore, $\mathcal{A}_0$ could be used as a reliable indicator of gas distribution in the field. In particular, the area in the vicinity of $x = 9$ km, $y = 3$ km possibly has significant gas reserves. The coefficient $\mathcal{A}_0$ should be sensitive to gas present in pores but not in vertical fractures; it could, therefore, serve as an indicator of gas accumulation within the pore space. It is interesting to note that the estimated quality factor of these gas sands can be as low as five (close to the values reported by Mavko and Dvorkin 2005). Such small

Q values are especially remarkable because $\mathcal{A}_0$ corresponds to the effective attenuation of the whole target layer that includes lithologies other than gas sands.

The inversion for the attenuation-anisotropy parameters $\delta_Q^{(1,2,3)}$ and $\varepsilon_Q^{(1,2)}$ appears to be ill-constrained because of the sensitivity of amplitude analysis to noise. This is evident from the lack of large-scale spatially coherent patterns of these parameters within the survey area (Figure 8b).

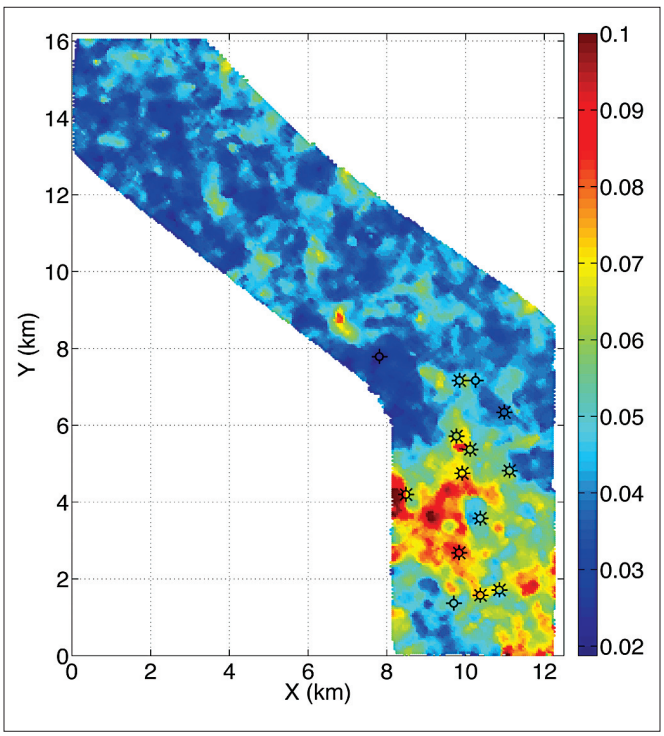

Figure 7. *Interval vertical attenuation coefficient $\mathcal{A}_0 = 1/(2Q_0)$ for the target layer. Location of gas-producing (circles with eight lines) and dry wells (circles with four lines) in Coronation Field (modified from Monk et al., 2006) are also marked.*

Well planning should take both interval velocity anisotropy and the attenuation coefficient into account. The optimal strategy would be to drill horizontal wells orthogonal to the fractures in the lower half of the survey area, where attenuation anomalies should correspond to gas accumulations.

Conclusions

P-wave anisotropic velocity and attenuation analysis provides valuable information for reservoir characterization at the Coronation Field. The interval traveltime and attenuation within a subsurface zone containing the reservoir sands were estimated using the layer-stripping approach introduced by Dewangan and Tsvankin (2006) and Behura and Tsvankin (2009a). Nonhyperbolic semblance analysis yielded the wide-azimuth traveltimes for reflections from the top and bottom of the reservoir. Then velocity-independent layer-stripping was employed to generate interval traveltime surfaces, which were inverted for the interval velocity-anisotropy parameters of orthorhombic media. The windowed events along the moveout surfaces were used for computing the interval anisotropic attenuation.

The lower half of the survey area shows strong azimuthal velocity anisotropy as well as high attenuation. Areas of large interval vertical attenuation coefficient $\mathcal{A}_0$ correlate with locations of gas-producing wells, which makes $\mathcal{A}_0$ a reliable indicator of gas sands in the field. In such high-attenuation areas, the orientation of the estimated NMO ellipses can be used to

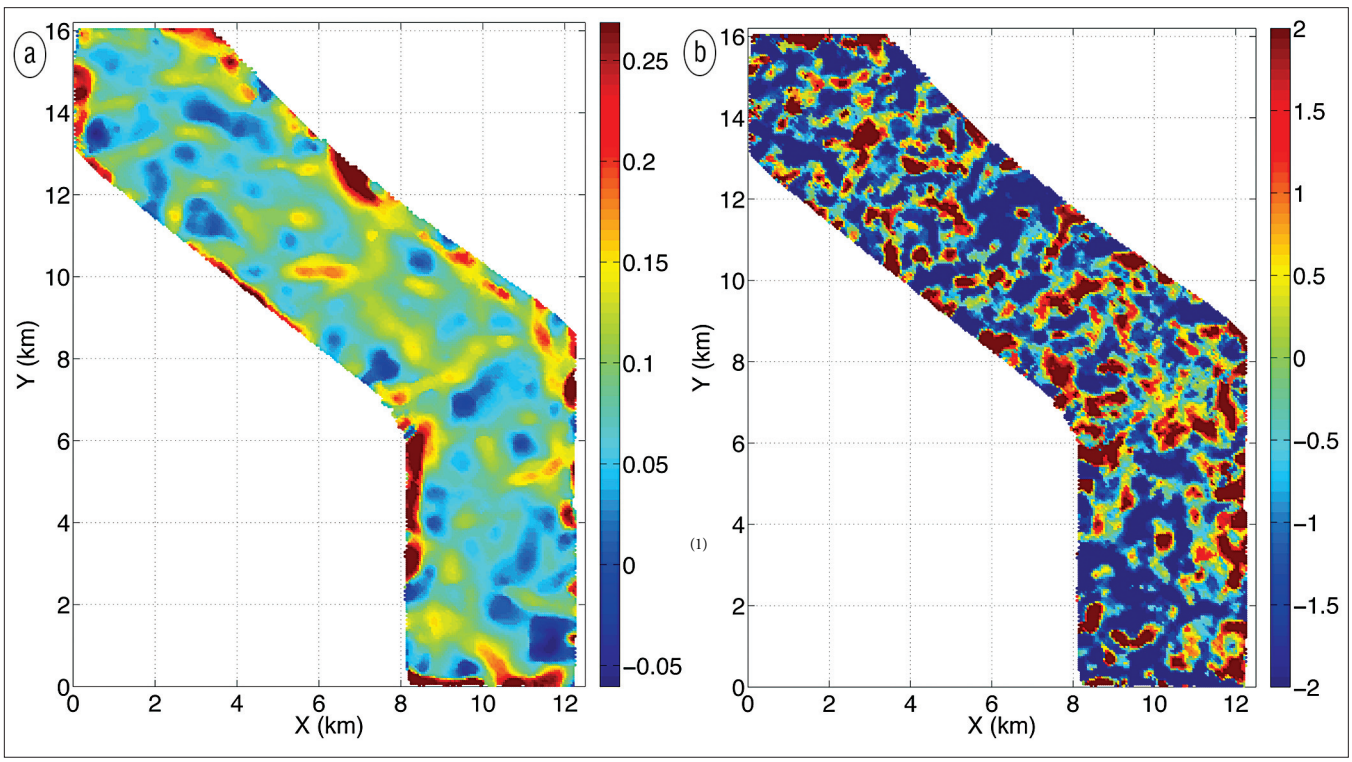

Figure 8. *(a) Velocity-anisotropy parameter $\delta^{(1)}$ and (b) attenuation-anisotropy parameter $\delta_Q^{(1)}$.*

plan horizontal wells, which should be orthogonal to the predominant fracture strike. TLE

References

Behura, J., M. Batzle, R. Hofmann, and J. Dorgan, 2009, The shear properties of oil shales: The Leading Edge, **28**, no. 7, 850–855, http://dx.doi.org/10.1190/1.3167788.

Behura, J., and I. Tsvankin, 2009a, Estimation of interval anisotropic attenuation from reflection data: Geophysics, **74**, no. 6, A69–A74, http://dx.doi.org/10.1190/1.3191733.

Behura, J., and I. Tsvankin, 2009b, Role of the inhomogeneity angle in anisotropic attenuation analysis: Geophysics, **74**, no. 5, WB177–WB191, http://dx.doi.org/10.1190/1.3148439.

Dewangan, P., and I. Tsvankin, 2006, Velocity-independent layer stripping of PP and PS reflection traveltimes: Geophysics, **71**, no. 4, U59–U65, http://dx.doi.org/10.1190/1.2210975.

Jackson, P. C., 1984, Paleogeography of the lower cretaceous mannville group of western Canada, *in* J. A. Masters, Elmworth: Case study of a deep basin gas field, AAPG Memoir, **38**, 49–77.

Mavko, G. M., and J. Dvorkin, 2005, P-wave attenuation in reservoir and non-reservoir rock: 67th EAGE Conference & Exhibition.

Mavko, G. M., and A. Nur, 1979, Wave attenuation in partially saturated rocks: Geophysics, **44**, no. 2, 161–178, http://dx.doi.org/10.1190/1.1440958.

Monk, D., R. Larson, and P. Anderson, 2006, An East-Central Alberta multi-component seismic case history: CSEG Recorder, 18–22.

Tsvankin, I., 1997, Anisotropic parameters and P-wave velocity for orthorhombic media: Geophysics, **62**, no. 4, 1292–1309, http://dx.doi.org/10.1190/1.1444231.

Wang, X. and I. Tsvankin, 2009, Estimation of interval anisotropy parameters using velocity-independent layer stripping: Geophysics, **74**, no. 5, WB117–WB127, http://dx.doi.org/10.1190/1.3157462.

Zhu, Y. and I. Tsvankin, 2007, Plane-wave attenuation anisotropy in orthorhombic media: Geophysics, **72**, no. 1, D9–D19, 17, http://dx.doi.org/10.1190/1.2387137.

Acknowledgments: We thank ION Geophysical and VGS Seismic for providing the field data and for permission to publish this work. Alex Calvert is currently with Maersk Oil.

Corresponding author: jbehura@mines.edu